



Ambient-temperature NO oxidation over amorphous $\text{CrO}_x\text{-ZrO}_2$ mixed oxide catalysts: Significant promoting effect of ZrO_2

Aiyong Wang^{a,b}, Yanglong Guo^{a,*}, Feng Gao^{b,*}, Charles H.F. Peden^b

^a Key Laboratory for Advanced Materials, Research Institute of Industrial Catalysis, East China University of Science and Technology, Shanghai 200237, PR China

^b Institute for Integrated Catalysis, Pacific Northwest National Laboratory, P.O. Box 999, Richland, WA 99352, United States

ARTICLE INFO

Article history:

Received 5 January 2016

Received in revised form 19 February 2016

Accepted 22 February 2016

Available online 24 February 2016

Keywords:

Oxide catalyst

NO oxidation

Ambient temperature oxidation

CrO_x

ZrO_2

ABSTRACT

A series of novel $\text{CrO}_x\text{-ZrO}_2$ mixed oxide catalysts are prepared via a sol-gel method. Within a range of Cr/Zr atomic ratios, the mixed oxides maintain high surface area, homogeneous amorphous phases. As compared to CrO_x -only catalysts formed using the same method, the addition of zirconia greatly enhances the catalytic performance for ambient-temperature, low-concentration NO oxidation. X-ray Photoelectron Spectroscopy (XPS) and Electron Paramagnetic Resonance (EPR) analyses indicate an electronic effect of ZrO_2 addition to the oxidation state of Cr. That is, ZrO_2 addition induces an increase in surface concentrations of Cr^{6+} . Rapid deactivation of a pre-reduced catalyst, coupled with the fact that a deactivated catalyst contains lower concentrations of surface Cr^{6+} , provide rather strong evidence for a Mars-van Krevelen NO oxidation mechanism. Such a mechanism is also consistent with in situ DRIFTS observations.

© 2016 Elsevier B.V. All rights reserved.

1. Introduction

The emission of nitrogen oxides (NO_x, mainly NO and NO₂) has increased dramatically during the past decades as a result of the rapid global economic growth. Nitrogen oxides have a significant negative influence on human health and the environment. Currently, NO_x generated from transportation is removed via on-board exhaust aftertreatment techniques, including three-way catalytic conversion, ammonia selective catalytic reduction (NH₃-SCR) and NO_x storage reduction (NSR) techniques [1–8]. However, complete elimination of NO_x is in general difficult to achieve, especially during the cold start periods. Tens of ppm of NO_x (predominately NO), as a result of incomplete NO_x removal by the above-mentioned methods, is typically accumulated in places where ventilation is inadequate, such as road tunnels and indoor parking. Forced ventilation is not only cost prohibitive, but also causes additional environment pollution. Since NO₂ can be readily absorbed in water or base solutions, a technology combining ambient temperature catalytic oxidation of low concentration NO to NO₂, followed by NO₂ absorption may be a viable approach to remove ppm-level NO_x in air.

Pt-based catalysts have shown good performance in the catalytic oxidation of NO [9,10]. However, due to their high cost and low activity at ambient temperatures, they are unsuitable for NO_x removal in road tunnels and indoor parking. Chromium oxide catalysts have been reported by Liu et al. for room temperature, low-concentration NO oxidation some time ago [11], however, with rather low activity and durability precluding any application potential. A few studies have reported good performance of MnO_x-based catalysts for low temperature SCR and NO oxidation [12–14]. Notably, Shi and coworkers [15,16] reported that X-Mn (X = Fe, Co, Ni, Zn) binary oxides display high activity in low concentration NO catalytic removal at room temperature. However, due to accumulation of nitrite and nitrate species on the surfaces of these binary oxides, they completely deactivate within a few hours of use. Recently, this same group reported that amorphous manganese oxides and Mg-doped manganese oxides display much improved ambient temperature NO removal performance, especially in the presence of moisture [17,18]. In one study, these authors demonstrated significant moisture-induced durability enhancement of their amorphous manganese oxides, from tens of hours to hundreds of hours of continuous application. This has been attributed to an inhibition effect of H₂O toward nitrate deposition, suggested to proceed via formation and removal of nitric acid vapor (i.e., $3\text{NO}_2 + \text{H}_2\text{O} = 2\text{HNO}_3 + \text{NO}$). However, these catalysts do not appear to sustain a thermal reactivation. As demonstrated by the authors, their best performing catalyst deactivates completely after annealing.

* Corresponding authors.

E-mail addresses: ylguo@ecust.edu.cn (Y. Guo), feng.gao@pnnl.gov (F. Gao).

ing to 200 °C for 6 h [17], casting doubts on their reusability. In another study, a series of Mg-doped manganese oxides were used for ambient temperature NO oxidation. In the absence of moisture, the best performing catalyst starts to deactivate rapidly after ~10 h of use. Again, in the presence of moisture, continuous application time extends to a few hundred hours. Catalyst reactivation was not reported in this study [18]. There has been no other report on catalysts with higher durability for low concentration NO oxidation at ambient temperature.

Herein, we report for the first time fully regenerable zirconia modified CrO_x catalysts exhibiting 100% conversion of low-concentration NO oxidation at 25 °C for long periods, which appears to be promising for practical applications. The effects from Cr/Zr ratio and calcination temperature to NO oxidation were systematically studied. The materials were further characterized with a number of spectroscopic methods in order to elucidate catalyst structure/function relationships and to obtain insight into the reaction mechanism. Even though this study is clearly application oriented, most of the NO oxidation tests were performed under “idealized” conditions; i.e., without the presence of H₂O and CO₂ in the feed, in order to better understand the nature and function of these novel catalysts. A more thorough study looking at durability of the catalysts under real-world conditions is currently underway. However, for our best performing catalyst, one preliminary test was conducted in the presence of moisture to further demonstrate its potential for practical applications.

2. Experimental

2.1. Catalyst preparation

The catalyst samples were synthesized with a sol-gel method, using equal moles of citric acid and metal nitrate as precursors. In a typical synthesis, a mixture of Cr(NO₃)₃·9H₂O and Zr(NO₃)₄·5H₂O (0.045 mol of metal in total), and citric acid (0.045 mol) were dissolved in 40 ml of deionized water. The solution was stirred at 70 °C for 3 h in air to form a sol-gel. The resultant sol-gel was dried at 80 °C overnight in an oven, forming a porous, foam-like solid. The solid samples were calcined at designated temperatures for 4 h in a muffle furnace. The calcined samples (i.e., the catalysts) are denoted here as Cr_xZr_y-T, where x/y represents the Cr/Zr molar ratio and T denotes the calcination temperature. The catalysts were ground, pressed and sieved to 40–60 mesh size before use in NO oxidation tests.

2.2. Catalytic activity measurement

The catalytic activity for NO oxidation was evaluated in a continuous flow fixed-bed quartz reactor with 8 mm I.D.; 0.4 g of catalyst was used in each test. The reaction temperature was maintained at 25 °C by a thermostatic water bath. For most reaction tests, the feed gas composition was as follows: 12 ppm NO, 21 vol.% O₂, and balance Ar. Under ambient conditions, the total flow rate was 300 ml/min and the GHSV (gas hourly space velocity) was 45000 ml g⁻¹ h⁻¹. Before experiments, the catalysts were pretreated at 300 °C for 1 h in 21% O₂/Ar (300 ml/min). After cooling to the reaction temperature at 25 °C, the gas flow was switched to the reactant feed, and the compositions of the inlet and outlet gases were monitored continuously using an on-line NO_x analyzer (Thermo Fisher 42i-LS). In one specific test, the Ar carrier gas was allowed to pass through a water reservoir to carry ~2.5% H₂O to the reaction feed. From the concentrations of the outlet gases, NO conversions are calculated according to the following equation:

$$\text{NO conversion (\%)} = \frac{\text{NO}_{\text{inlet}} - \text{NO}_{\text{outlet}}}{\text{NO}_{\text{inlet}}} \times 100$$

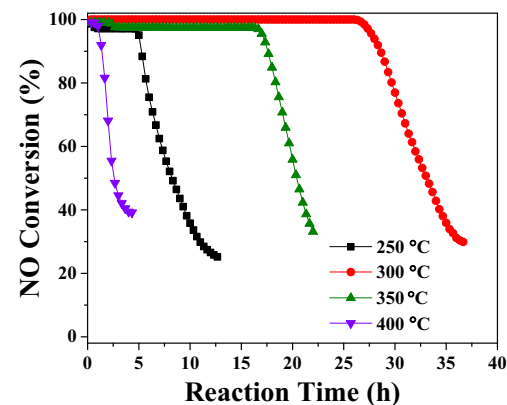


Fig. 1. NO conversion as a function of reaction time on Cr₈Zr₁ catalysts calcined at different temperatures. The reactant feed contains 12 ppm of NO, 21% of O₂ balanced with Ar at a GHSV of 45,000 ml g⁻¹ h⁻¹ and a reaction temperature of 25 °C.

where subscripts *inlet* and *outlet* indicate the inlet and outlet NO concentrations, respectively.

2.3. Catalyst characterizations

A Micromeritics ASAP 2020 Accelerated Surface Area and Porosimetry Analyzer was used to measure the N₂ adsorption/desorption isotherms at 77 K. Before the measurements, all catalysts were outgassed at 200 °C for 500 min under flowing N₂. The Brunauer–Emmett–Teller (BET) method was used to calculate the specific surface areas. Pore volume and pore size distribution were obtained from the Barrett–Joyner–Halenda (BJH) method.

X-ray powder diffraction (XRD) measurements were performed on a Bruker AXS D8 focus diffractometer with CuK α radiation (40 kV, 40 mA, λ = 1.5406 Å) and the diffraction patterns were collected over a 2θ range of 10–80° at the scanning rate of 6 min⁻¹, with a 0.02° step size.

X-ray photoelectron spectroscopy (XPS) spectra were recorded using a Thermo ESCALAB 250 electron spectrometer with a monochromatic AlK α X-ray resource (1486.6 eV) and a pass energy of 30 eV. All binding energies were referenced to the C 1s line of adventitious carbon at 284.8 eV.

The temperature-programmed desorption of NO_x (NO_x-TPD) was tested in the 25–300 °C temperature range. Prior to measurements, the catalysts were first pretreated under 21 vol.% O₂/Ar (300 ml/min) mixed gas at 300 °C for 1 h. The catalysts were then exposed to a 300 ml/min flow of 500 ppm NO in Ar at 25 °C for 90 min, and purged with Ar for 1 h. The TPD experiments were conducted at a ramping rate of 5 K/min; the evolved gases were recorded by the NO_x analyzer.

In situ Diffuse Reflectance Infrared Fourier Transform (DRIFT) spectra were acquired with a Nicolet 6700 infrared spectrometer. Prior to each measurement, the catalysts were heated in 50 ml/min 21 vol.% O₂/Ar to 300 °C, held at this temperature for 1 h to remove impurities. Then, the catalysts were cooled to 25 °C to carry out the adsorption of NO (500 ppm NO, 21 vol.% O₂, balance Ar) for different periods. The spectra were recorded with 50 scans at a spectral resolution of 4 cm⁻¹, using single beam spectra of clean catalysts measured at 25 °C in a flow of 21 vol.% O₂/Ar as backgrounds.

3. Results and discussion

The effect of calcination temperature on the NO oxidation performance of the Cr₈Zr₁ mixed-oxide catalysts was studied first, and the results are shown in Fig. 1. This shows that the catalytic performance depends dramatically on calcination temperature. Among

Table 1

Effect of calcination temperature on surface areas, pore volumes and pore diameters of the Cr8Zr1 catalysts.

sample	S_{BET} (m^2/g)	Micropore surface (m^2/g)	Micropore volume (cm^3/g)	Pore volume (cm^3/g)	Average pore diameter (nm)
Cr8Zr1-250	226	166	0.09	0.11	2.42
Cr8Zr1-300	389	155	0.07	0.17	2.66
Cr8Zr1-350	185	0	0	0.09	3.23
Cr8Zr1-400	124	0	0	0.14	3.79

the four catalysts, Cr8Zr1-300 performs the best where NO conversion maintains at 100% for nearly 26 h. Inferior performance is observed for the Cr8Zr1-250 and Cr8Zr1-350 catalysts, where 100% NO conversion maintains for 5 and 15 h, respectively. The performance of Cr8Zr1-400, on the other hand, is much worse than the other three. To elucidate the dramatic effect on catalyst calcination temperature, Fig. 2 presents XRD patterns of the four Cr8Zr1 mixed-oxide catalysts. Cr8Zr1-250, Cr8Zr1-300 and Cr8Zr1-350 catalysts exhibit amorphous structures while the Cr8Zr1-400 catalyst displays sharp Cr_2O_3 XRD peaks (ICDD PDF #84-1616, $\theta = 33.6, 54.9, 36.3^\circ$). BET surface areas and pore characteristics of the samples are summarized in Table 1. With increasing calcination temperature, the BET surface areas of the mixed-oxides first increase, reaching the highest value at 300 °C, and then decrease. However, pore volumes and average pore diameters of the catalysts keep increasing with increasing calcination temperature. These initial results demonstrate some correlation between catalytic activity and surface area/crystallinity of the catalysts. For example, the best performance for Cr8Zr1-300 could be related to its highest surface area. Note, however, Cr8Zr1-250 has somewhat higher surface area than Cr8Zr1-350, yet its catalytic performance is considerably inferior. This suggests that catalyst calcination temperature affects both the nature and the availability of surface active sites for NO oxidation. For the Cr8Zr1-400 catalyst, it is anticipated that either the density, or the activity of surface active sites, or both, are substantially inferior to other three catalysts.

Since it is rather obvious that a calcination temperature of 300 °C results in catalysts with good performance, a series of Cr-Zr mixed-oxides with varying Cr/Zr molar ratios were prepared using this calcination temperature, and Fig. 3 shows their NO oxidation catalytic performance at 25 °C. Cr and Zr-only catalysts were also prepared for comparison. All catalysts except Zr-300 (which is completely inert) show 100% initial NO conversions. With reaction time, however, significant differences are observed: catalytic performance increases first with increasing zirconium content and an optimum catalytic performance is found for Cr8Zr1-300. Further increases in Zr content result in a decline in catalytic performance.

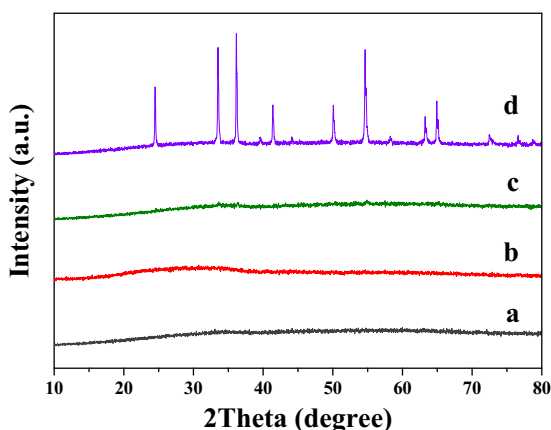


Fig. 2. XRD patterns of the Cr8Zr1 mixed-oxide catalysts calcined at different temperatures: (a) 250 °C; (b) 300 °C; (c) 350 °C; (d) 400 °C.

To gain a better understanding of the NO catalytic oxidation process and possible reaction mechanisms on the Cr-Zr mixed-oxide catalysts, Fig. 4 displays outlet NO, NO_2 and NO_x ($\text{NO} + \text{NO}_2$) concentrations as a function of reaction time tested on the series of Cr-Zr mixed-oxide catalysts with different Cr/Zr molar ratios calcined at 300 °C. For all of the mixed-oxide catalysts, NO_x outlet can be divided into 4 stages. In stage I (the first 30–60 min), no NO_x desorption is observed. In stage II, NO_x (solely NO_2) breaks through and reaches 10–12 ppm over the course of a few hours. In stage III, NO_x (solely NO_2) slightly fluctuates, but largely maintains at ~12 ppm. Finally in stage IV, NO breaks through and NO_x (NO and NO_2) outlet concentrations maintain exactly at 12 ppm. Primarily, the length of stage III best describes catalytic performance, where Cr8Zr1-300 and Cr12Zr1-300 clearly excel over the others. For Cr-300, besides its inferior overall performance, this catalyst does not display a clear stage I. These results demonstrate that all mixed oxide catalysts have some NO_x storage capacities (stages I and II). NO_x storage does not immediately inhibit NO oxidation due to low reactant concentrations. With time, all catalysts deactivate. The NO_x storage capacities of the catalysts (measured from the beginning of the experiment to the point NO_2 outlet concentration first reaches 10 ppm) are calculated and the results are displayed in Table 2. The mixed-oxide catalysts show comparable NO_x storage capacities to the generally used NO_x storage materials, such as $\text{Pt}/\text{Al}_2\text{O}_3$, $\text{Ba}/\text{Al}_2\text{O}_3$ and Ba/TiO_2 [19–21].

Fig. 5 presents XRD patterns of the series of catalysts used to generate data shown in Figs. 3 and 4. Only Cr-300 (Fig. 5a) is crystallized, corresponding to Cr_2O_3 (ICDD PDF #84-1616 $\theta = 33.6^\circ, 54.9^\circ, 36.3^\circ$), while all of the other catalysts are amorphous. These results clearly demonstrate that the CrxZry-300 samples are not physical mixtures of Cr-300 and Zr-300 but instead are new homogeneous amorphous phases. It is significant that even a small amount of Zr (e.g., Cr/Zr = 16) is sufficient to generate such amorphous mixed oxides.

Table 3 presents BET surface areas and pore characteristics of the series of catalysts calcined at 300 °C during synthesis, where microporous volumes were determined by the t-plot method. The

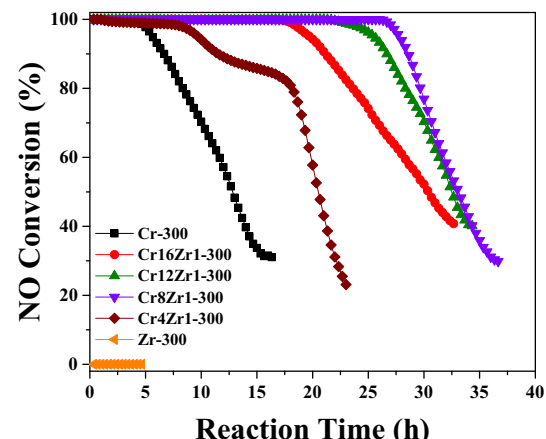


Fig. 3. NO conversion as a function of reaction time on CrxZry-300 and Cr (or Zr)-300. The reactant feed contains 12 ppm of NO, 21% of O_2 balanced with Ar at a GHSV of 45,000 $\text{ml g}^{-1} \text{h}^{-1}$ and a reaction temperature of 25 °C.

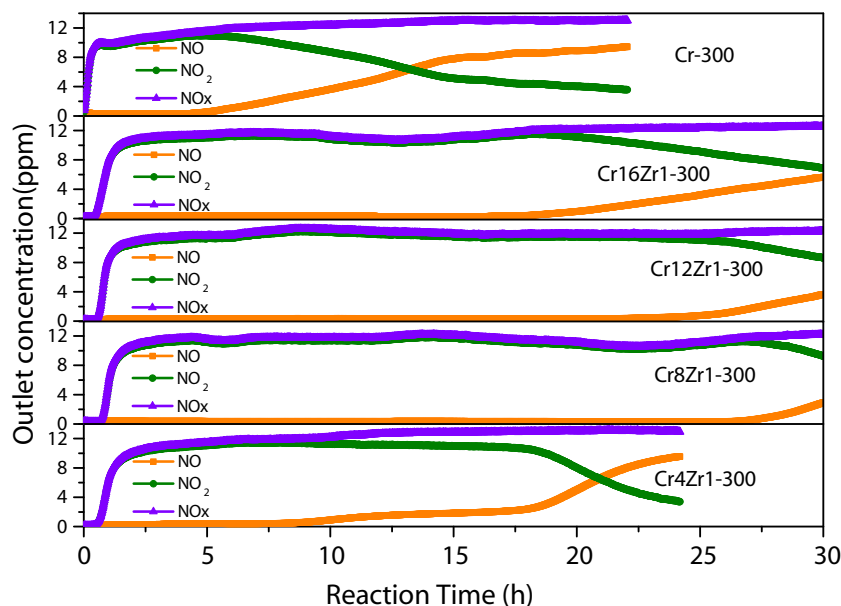


Fig. 4. Outlet NO and NO₂ concentrations as a function of time during the NO oxidation tests on CrxZry-300 and Cr-300. The reactant feed contains 12 ppm of NO, 21% of O₂ balanced with Ar at a GHSV of 45,000 ml g⁻¹ h⁻¹ and a reaction temperature of 25 °C.

Table 2

NO_x storage capacity of the CrxZry-300 and Cr (or Zr)-300 catalysts.

Sample	Cr-300	Cr16Zr1-300	Cr12Zr1-300	Cr8Zr1-300	Cr4Zr1-300	Zr-300
NO _x storage amount (μmol/g _{cat})	3.3	15.8	16.0	19.4	19.0	0

Table 3

Surface areas, pore volumes and pore diameters of the CrxZry-300 and Cr (or Zr)-300 catalysts.

sample	S _{BET} (m ² /g)	Microporous surface (m ² /g)	Microporous volume (cm ³ /g)	Porous volume (cm ³ /g)	Average pore diameter (nm)
Cr-300	194	35	0.01	0.12	3.7
Cr16Zr1-300	301	39	0.02	0.18	3.0
Cr12Zr1-300	351	42	0.03	0.20	2.9
Cr8Zr1-300	389	155	0.07	0.17	2.7
Cr4Zr1-300	330	147	0.06	0.16	3.2
Zr-300	9	–	–	–	6.4

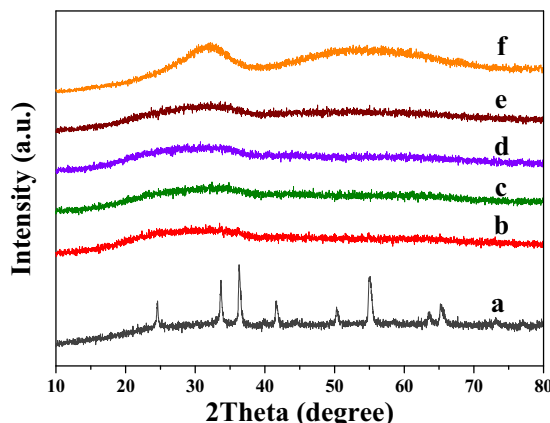


Fig. 5. XRD patterns of CrxZry-300 and Cr (or Zr)-300: (a) Cr-300; (b) Cr16Zr1-300; (c) Cr12Zr1-300; (d) Cr8Zr1-300; (e) Cr4Zr1-300; (f) Zr-300.

average pore diameters of the Cr-Zr mixed-oxides decrease from 3.0, 2.9 to 2.7 nm, for Cr16Zr1-300, Cr12Zr1-300, and Cr8Zr1-300, respectively. Further increase in Zr/Cr ratio leads to an increase in average pore diameter (3.2 nm for Cr4Zr1-300). For the single-metal oxides, Cr-300 and Zr-300, relatively large pore sizes (3.7 and

6.4 nm, respectively) are observed. It can be seen that the mixed oxides have larger BET surface areas and smaller pore volumes than the single-metal oxides. However, again, no clear correlation can be made between these parameters and the NO oxidation performance. For example, the catalytic performance for Cr4Zr1-300 is clearly inferior to the other three mixed oxides, yet all 4 of them have rather similar surface areas and pore characteristics; Cr4Zr1-300 even has the largest average pore openings and is, thus, perhaps less vulnerable to poisoning from nitrate deposition. This indicates that the nature of the catalytically active sites play a more important role in determining catalytic performance.

Since the catalysts described here are application driven, and since all catalysts deactivate with time, it is important to investigate their regeneration. As shown in Fig. 6, after treating a fully deactivated Cr8Zr1-300 (used for 50 h in NO oxidation) in a 300 ml/min 21 vol.% O₂/Ar flow for 1 h at 300 °C, the performance of the catalyst is essentially fully regenerated.

The reaction mechanism for ambient temperature NO oxidation on an oxide catalyst has not been clearly established. However, the two most likely candidates are a Langmuir–Hinshelwood mechanism, where NO reacts with chemisorbed O₂, or a Mars–van Krevelen mechanism where NO reacts with surface lattice oxygen, which is thereafter replenished by chemisorbed O₂. A major difference between the two mechanisms is that in the latter, redox of the

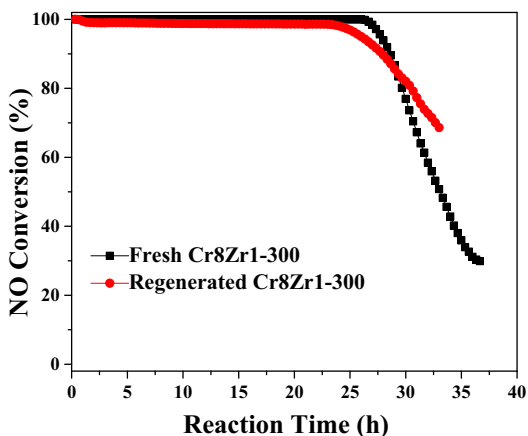


Fig. 6. NO conversion as a function of reaction time on fresh and regenerated Cr8Zr1-300. The reactant feed contains 12 ppm of NO, 21% of O₂ balanced with Ar at a GHSV of 45,000 ml g⁻¹ h⁻¹ and a reaction temperature of 25 °C.

surface cationic sites is part of the reaction mechanism. In order to gain insights into possible reaction mechanism, especially whether oxidation states of surface cationic sites have an effect on NO oxidation performance, in the following the Cr8Zr1-300 was pretreated by reduction before use. In particular, the Cr8Zr1-300 catalyst was reduced in 5 vol% H₂ in Ar at 120 °C for 1 h, and then cooled to 25 °C to carry out NO oxidation. Interestingly, as shown in Fig. 7, following a short complete NO_x storage stage (~40 min), NO conversion decreases rapidly with reaction time, reaching a lowest point at ~2.2 h. During this stage, no NO₂ is detected in the outlet. After a reaction time of ~2.2 h, NO conversion increases again, reaching ~100% NO conversion again by a reaction time of ~3 h. In this stage, NO outlet concentration decreases with time while NO₂ outlet concentration quickly increases. These results indicate at least two things: (1) certain active sites in the reduced catalyst deactivate very rapidly; and (2) new active sites are generated as the reaction proceeds. Since a catalyst reduction treatment most certainly alters oxidation states of surface Cr and (perhaps) Zr sites, results shown in Fig. 7 strongly indicate a connection between reactivity and oxidation states of surface cationic sites. Note that the catalyst self-activation stage (reaction time ~2.2–3 h) is accompanied with gas-phase NO₂ formation and NO₂ is a stronger oxidant than O₂. This self-activation, therefore, is likely associated with oxidation of surface cationic sites. In the next experiments, XPS and EPR are

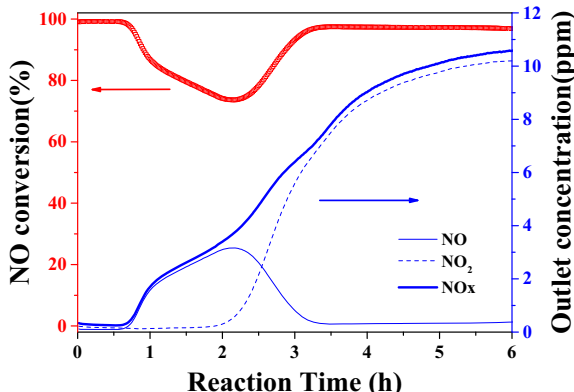


Fig. 7. NO conversion as a function of reaction time (red line) and outlet NO and NO₂ concentrations (blue lines) during the NO oxidation test on a 5 vol% H₂/Ar pretreated Cr8Zr1-300 catalyst. The reactant feed contains 12 ppm of NO, 21% of O₂ balanced with Ar at a GHSV of 45,000 ml g⁻¹ h⁻¹ and a reaction temperature of 25 °C. (For interpretation of the references to color in this figure legend, the reader is referred to the web version of this article.).

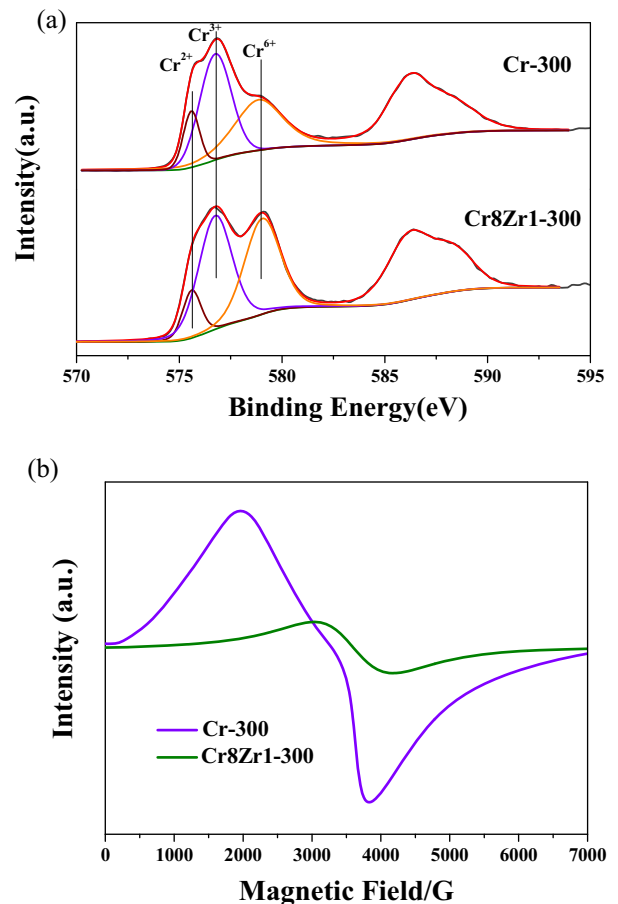


Fig. 8. (a) Cr 2p XPS spectra for Cr-300 and Cr8Zr1-300. (b) EPR spectra obtained at room temperature for Cr-300 and Cr8Zr1-300.

utilized to gain more insights into the electronic properties of the catalysts. Experiments were performed by comparing the highly active Cr8Zr1-300 catalyst and its Zr-free counterpart, Cr-300.

Fig. 8a shows the Cr 2p XPS spectra of the Cr-300 and Cr8Zr1-300 catalysts. Two groups of features, at 574–582 eV (assigned to Cr 2p_{3/2}) and 584–592 eV (assigned to Cr 2p_{1/2}), were observed. Using the same peak deconvolution method, three Cr 2p_{3/2} peaks for the Cr-300 and Cr8Zr1-300 catalysts, centered at ~575.6, 576.7 and 579.0 eV, are obtained. Based on literature, these features can be assigned to Cr²⁺, Cr³⁺ and Cr⁶⁺, respectively [22–25]. It is obvious that Cr8Zr1-300 contains much higher concentrations of surface Cr⁶⁺ as compared to Cr-300, demonstrating that ZrO₂ doping significantly stabilizes surface Cr⁶⁺ ions, indicating that Zr⁴⁺ not only functions to stabilize catalyst structure, but also an electronic promoter. Table 4 lists the binding energies (in eV) and the distribution of different valence states of Cr⁴⁺ in both catalysts. It has been reported in literature that Cr⁵⁺ exhibits a binding energy at 578.0–578.8 eV [26,27]. This feature does not appear to be present in our catalysts.

The EPR spectra of pure Cr-300 and Cr8Zr1-300 are shown in Fig. 8b. In these catalysts, only Cr²⁺ and Cr³⁺ are EPR active due to the presence of unpaired electrons for these oxidation states [28]. The stronger signal intensity of Cr²⁺ and Cr³⁺ in Cr-300 again demonstrates that ZrO₂ stabilizes Cr⁶⁺. Since XPS is surface sensitive while EPR is a bulk technique, the combination of Fig. 8a and b suggests that ZrO₂ doping increases both surface and bulk Cr⁶⁺ concentrations. As will be shown below, the enrichment of surface Cr⁶⁺ in Cr8Zr1-300 correlates directly with its higher NO oxidation activity.

Table 4
XPS of Cr 2p in Cr-300 and Cr8Zr1-300.

XPS spectra	Element valence	Binding energies (percent of valence state, %)	
		Cr-300	Cr8Zr1-300
Cr 2p (eV) concentration(%)	Cr ²⁺	575.6 (13.5)	575.6 (10.9)
	Cr ³⁺	576.8 (51.9)	576.7 (46.9)
	Cr ⁶⁺	578.9 (34.6)	579.0 (42.2)

As illustrated in [Figs. 1 and 3](#), all of the catalysts deactivate with time. This can be caused by degrading of the active sites, i.e., from more active states to less active states during use, or by poisoning of the active sites, for example by deposits. Results shown in [Fig. 6](#), on the other hand, demonstrate that a simple thermal oxidation treatment completely regenerates a deactivated catalyst. To gain more insights into catalyst deactivation, Cr 2p_{3/2}, Zr 3d_{5/2} and O 1s XPS spectra for the fresh, deactivated (catalyst operated for 50 h in NO oxidation) and regenerated (catalyst operated for 50 h and then heated in 21 vol.% O₂/Ar (300 ml/min) mixed gas at 300 °C for 1 h) Cr8Zr1-300 catalyst were obtained. Cr 2p, Zr 3d and O1s features are displayed in [Fig. 9a–c](#), respectively. Peak fitting is carried out for Cr 2p_{3/2}, Zr 3d_{5/2} and O 1s, and the binding energies and distribution

of these ions are detailed in [Table 5](#). For all of the fresh, deactivated and regenerated Cr8Zr1-300, the Cr 2p_{3/2} spectra can again be best fit with three peaks centered at ~575.6, 576.7, and 579.0 eV, corresponding to Cr²⁺, Cr³⁺ and Cr⁶⁺, respectively. For the Zr 3d_{5/2} spectra, only one peak was obtained at ~182.0 eV, corresponding to Zr⁴⁺ [29]. For the O 1s spectra, three characteristic peaks were obtained. The peak at 529.9–523.0 eV corresponds to lattice oxygen (O²⁻) whereas the one at 531.1–531.2 eV can be assigned to chemisorbed oxygen on the catalyst surface, and/or oxygen in surface hydroxyl and carbonate moieties [30–32]. The higher binding energy state at 532.6–532.8 eV is attributed to oxygen in surface nitrate and/or nitrite [33,34]. It is important to note from [Fig. 9a](#) that both the fresh and regenerated catalysts contain higher concentra-

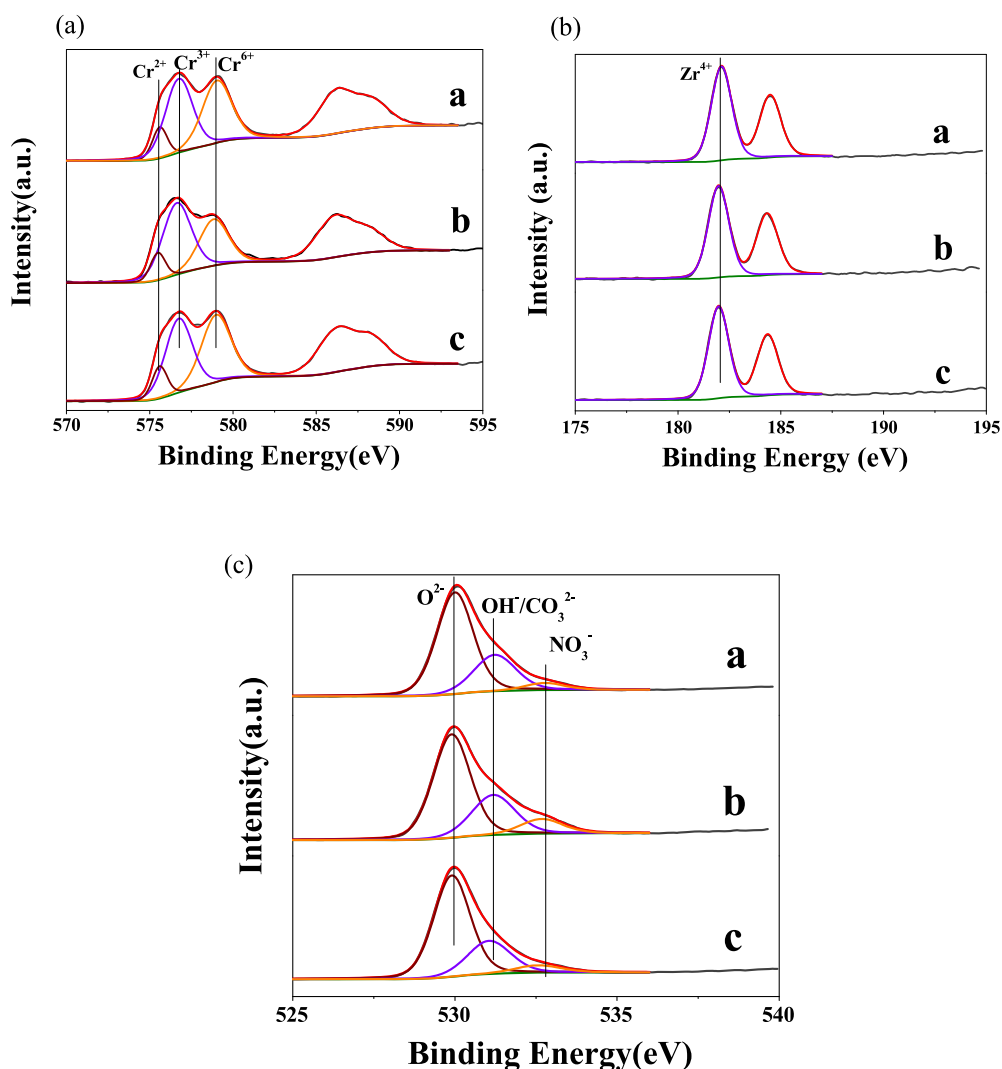


Fig. 9. (a) Cr 2p, (b) Zr 3d and (c) O 1s XPS spectra for the fresh, deactivated and regenerated Cr8Zr1-300 catalysts.

tions of surface Cr^{6+} compared to the deactivated catalyst. As can be seen from Fig. 9b, there is no obvious difference between the fresh and deactivated catalysts for $\text{Zr} 3d_{5/2}$, which indicates that Zr^{4+} primarily functions as a promoter. Finally, O1s spectra displayed in Fig. 9c demonstrate that after the NO oxidation test, the surface concentration for NO_3^- and/or NO_2^- increases at the expense of O^{2-} on the deactivated catalyst, suggesting involvement of lattice oxygen in NO oxidation. This, in turn, further indicates changes of the oxidation states of chromium ions during NO oxidation, as well as surface NO_3^- and/or NO_2^- formation being responsible for catalyst deactivation [35,36].

Based on a few key observations described above, especially rapid deactivation and self-activation of a reduced $\text{Cr}_8\text{Zr}_1\text{-}300$ catalyst (Fig. 7) and the involvement of lattice oxygen in NO oxidation (Fig. 9c), it is likely that NO oxidation on the mixed oxides studied here follows a Mars-van Krevelen (redox) mechanism where lattice oxygen bound to Cr^{6+} reacts with NO to form NO_2 , during which step Cr^{6+} is reduced to $\text{Cr}^{2+}/\text{Cr}^{3+}$. Thereafter $\text{Cr}^{2+}/\text{Cr}^{3+}$ is reoxidized to Cr^{6+} to finish redox cycling. A key mechanism for catalyst deactivation, again based on XPS observations, is the strong interaction between $\text{Cr}^{2+}/\text{Cr}^{3+}$ and surface nitrate/nitrite moieties which hinders continuous redox cycling. These mechanisms provide a satisfactory explanation to the “V”-shape NO conversion curve shown in Fig. 6 where the rapid deactivation stage can be understood via poisoning of surface $\text{Cr}^{2+}/\text{Cr}^{3+}$ by nitrate/nitrite and the self-activation stage can be attributed to $\text{Cr}^{2+}/\text{Cr}^{3+}$ oxidation to Cr^{6+} , likely by NO_2 .

Next, *in situ* DRIFT spectroscopy was applied to gain direct information about the evolution of reaction intermediates along with side products during NO oxidation. Fig. 10a illustrates the evolution of IR features recorded on the fresh $\text{Cr}_8\text{Zr}_1\text{-}300$ catalyst as a function of exposure time at 25°C . At low exposure times, two bands at ~ 1610 and $\sim 1290 \text{ cm}^{-1}$ dominate. According to literature assignments, a pair of bands at $1610\text{--}1620 \text{ cm}^{-1}$ and $1200\text{--}1220 \text{ cm}^{-1}$ can be assigned to the v_3 split vibration of bridge nitrates, whereas the band at 1290 cm^{-1} can be assigned to weakly adsorbed NO_2 [31,36]. Weaker features found at ~ 1450 and 1050 cm^{-1} are attributed to both components of the split v_3 vibration for nitrito Cr-ONO [37,38]. A broad band at $\sim 1520\text{--}1570 \text{ cm}^{-1}$ can be assigned to the stretching vibration of bidentate nitrates on the catalysts [39–41]. Finally, a weak band at $\sim 1680 \text{ cm}^{-1}$ is due to weakly adsorbed NO [37,42]. With increasing exposure time, it is seen that the relative intensity of the bidentate nitrates increases and becomes comparable to that of the bridge nitrates. In contrast, the intensity ratio between surface nitrito and adsorbed NO_2 remains relatively unchanged with exposure time. When comparing the intensities of weakly adsorbed NO and NO_2 , it is found that the intensity of weakly adsorbed NO_2

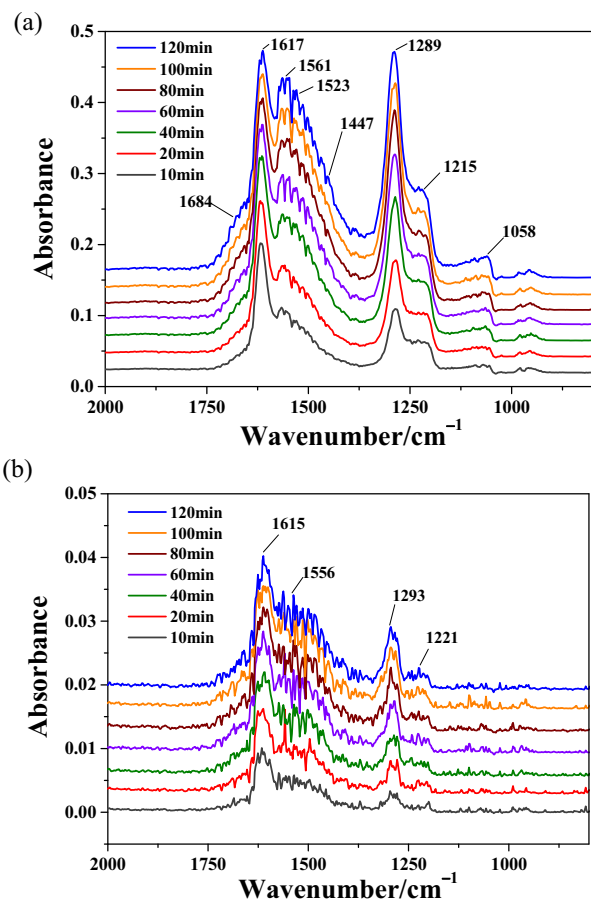


Fig. 10. Sequence of *in situ* DRIFT spectra recorded during NO oxidation on (a) $\text{Cr}_8\text{Zr}_1\text{-}300$ and (b) Cr-300 catalysts at 25°C .

is much stronger than that of NO. This indicates facile interaction between NO and surface oxygen to form NO_2 . The detection of Cr-ONO may indicate surface nitrito being an intermediate in NO oxidation, but this cannot be fully justified using DRIFTS alone. Fig. 10b shows the spectra of Cr-300 obtained under identical conditions. The lineshapes of the spectra are similar to those obtained on $\text{Cr}_8\text{Zr}_1\text{-}300$, yet with much lower intensities. This is consistent with the considerably lower activity for Cr-300.

NO and NO_2 TPD results are shown in Fig. 11a and b, respectively, for $\text{Cr}_8\text{Zr}_1\text{-}300$ and Cr-300 catalysts after saturation with NO at 25°C . For the $\text{Cr}_8\text{Zr}_1\text{-}300$ catalyst, three NO desorption states

Table 5

Binding energies (eV) and quantifications of Cr 2p, Zr 3d and O 1s in $\text{Cr}_8\text{Zr}_1\text{-}300$.

XPS spectra	Element valence	Binding energies (percent of valence state, %)		
		Fresh catalyst	Used catalyst	Regenerated catalyst
Cr 2p (eV) concentration(%)	Cr^{2+}	575.6 (10.9)	575.5 (10.8)	575.6 (11.0)
	Cr^{3+}	576.7 (46.9)	576.6 (53.8)	576.8 (44.7)
	Cr^{6+}	579.0 (42.2)	578.8 (35.4)	579.0 (44.3)
Zr 3d (eV) concentration(%)	Zr^{4+}	182.1	182.0	182.0
		–	–	–
O 1s (eV) concentration(%)	O^{2-}	530.0 (67.3)	529.9 (62.2)	529.9 (67.8)
	$\text{OH}^-/\text{CO}_3^{2-}$	531.2 (27.7)	531.2 (27.9)	531.1 (26.1)
	$\text{NO}_3^-/\text{NO}_2^-$	532.8 (5.0)	532.7 (9.9)	532.6 (6.1)

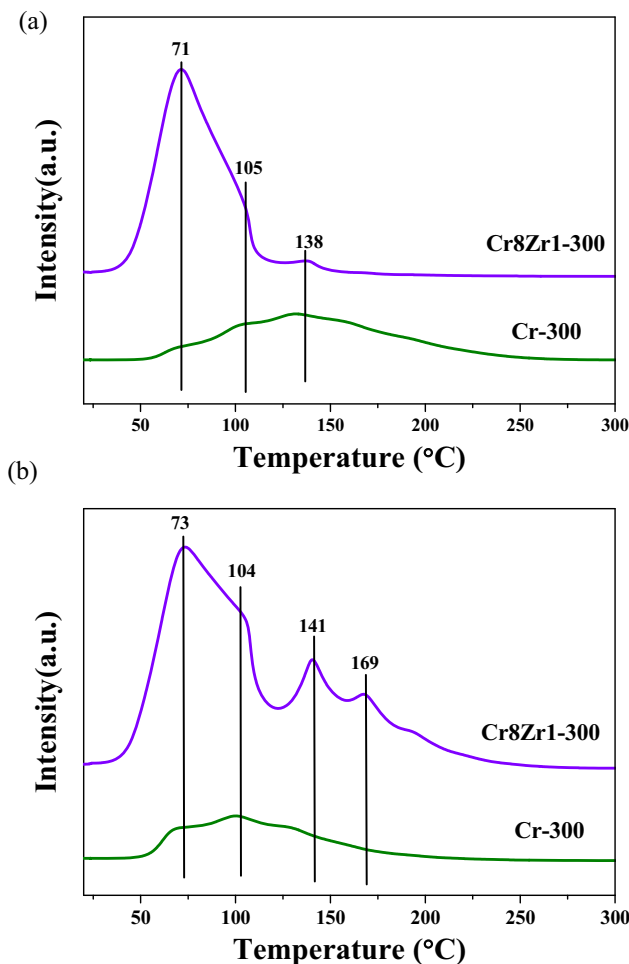


Fig. 11. Desorption profiles of (a) NO and (b) NO₂ during NOx-TPD of NO saturated Cr8Zr1-300 and Cr-300 catalysts.

are found: a strong feature at ~ 70 °C, and two much weaker states at 105 (as a shoulder of the low temperature state) and 138 °C. In contrast, NO₂ desorbs in more (and more distinct) temperature regimes, and desorption extends to much higher temperatures. The two low temperature states have desorption temperatures very similar to NO desorption, suggesting a rather symmetric transition state such that reaction intermediates (likely an nitrito) have similar probabilities to desorb as NO and NO₂. On the other hand, higher temperature NO₂ desorption (above ~ 120 °C) is due primarily to nitrate decomposition because of the lack of NO desorption counterparts. Nitrate thermal stability is fully consistent with its role as a reaction inhibitor as discussed above. The NO desorption peaks from Cr-300 are much weaker and extend to higher temperatures than Cr8Zr1-300, illustrating that the surface nitrogen-containing compounds bind stronger with the surface of Cr-300. Overall, with the introduction of zirconium, NO and NO₂ desorption yields increase significantly, especially at 71–73 °C, indicating that the mixed-oxide catalysts accelerate the adsorption of NO, the reaction of adsorbed NO with surface oxygen, and the desorption of NO₂.

Finally, to demonstrate the durability of our mixed oxides under more realistic conditions, Fig. 12 presents NO conversion as a function of reaction time over fresh Cr8Zr1-300 in the presence of H₂O. In this case, $\sim 2.5\%$ H₂O was introduced to the reactant by passing Ar through a bubble generator. As compared to Fig. 6, H₂O induces two key differences worthwhile noting: (1) 100% NO conversion is no longer achievable, even at the beginning of the

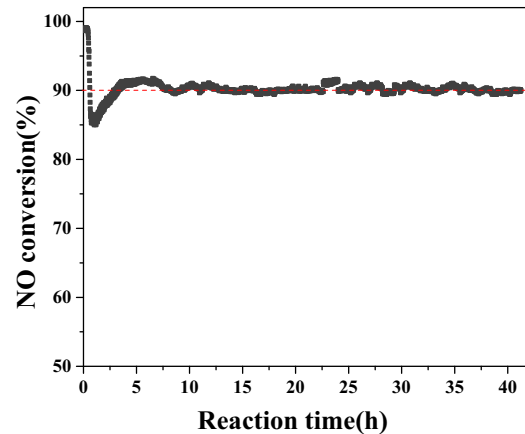


Fig. 12. NO conversion as a function of reaction time on fresh Cr8Zr1-300 in the presence of moisture. The reactant feed contains 12 ppm of NO, $\sim 2.5\%$ H₂O, 21% of O₂ balanced with Ar at a GHSV of $45,000 \text{ ml g}^{-1} \text{ h}^{-1}$ and a reaction temperature of 25 °C.

test; and (2) $\sim 90\%$ NO conversion maintains throughout the test time (slightly longer than 40 h), there being no sign for catalyst deactivation during this extended period. This preliminary assessment of durability clearly demonstrates that our catalysts do not suffer from rapid deactivation by water vapor. A likely explanation, as suggested recently by Shi and coworkers [17], is that H₂O inhibits nitrate deposition by reacting with NO₂ to form nitric acid vapor ($3\text{NO}_2 + \text{H}_2\text{O} = 2\text{HNO}_3 + \text{NO}$), which is readily carried away. This chemistry also explains why 100% NO conversion becomes unachievable in the presence of H₂O. As described in the introduction, the Mn-based catalysts, which also benefit from this inhibition effect, may suffer from activity loss during thermal regeneration [17,18]. It is clearly demonstrated here, however, that our Cr-based mixed oxides can be fully regenerated thermally (Fig. 6). A more detailed study is underway to further probe effects from H₂O and CO₂, species that are commonly found to deactivate oxide-based NO oxidation catalysts.

4. Conclusions

Novel Cr-Zr mixed oxides with high surface areas and high catalytic activity for the catalytic oxidation of low-concentration NO at ambient temperature are described. For the most active Cr8Zr1-300 catalyst prepared by a sol-gel method at 80 °C and calcined at 300 °C, 100% low-concentration (12 ppm) NO conversion is sustained for almost 26 h under a flow condition of $45000 \text{ ml g}^{-1} \text{ h}^{-1}$. This catalyst can be readily regenerated for reuse. Compared with the crystallized Cr-only catalyst, the mixed-oxide catalysts possess amorphous single-phase structures with high BET surface areas. XPS and EPR analyses reveal that ZrO₂ doping increases concentrations of surface Cr⁶⁺, key redox sites that facilitate NO oxidation. This notion is further supported by NOx-TPD and in situ DRIFTS measurements, which show that the addition of zirconium generates more active sites for NO oxidation. A "V"-shaped NO conversion curve on a pre-reduced catalyst provides strong indication for a redox NO oxidation mechanism, as well as a nitrite/nitrate poisoning deactivation mechanism. Overall, this study demonstrates that Cr-Zr mixed oxides possess high and steady NO oxidation activities at ambient temperature. This catalytic process, when coupled with an NO₂ absorption technology, holds great potential for low-concentration NOx removal from air, in locations such as road tunnels and indoor parking where other methods are not practical or economical. Studies on (1) the applicability of these mixed oxides under more realistic conditions, and (2) effects from other oxide cocatalysts are currently underway.

Acknowledgements

This work was supported by National Basic Research Program of China (2013CB933200), National Natural Science Foundation of China (21577035, 21577034), Commission of Science and Technology of Shanghai Municipality (15DZ1205305) and 111 Project (B08021). Aiyong Wang gratefully acknowledges the China Scholarship Council for the Joint-Training Scholarship Program with the Pacific Northwest National Laboratory (PNNL). PNNL is operated for the U.S. Department of Energy (DOE) by Battelle. FG and CHFP are supported by the U.S. DOE/Office of Energy Efficiency and Renewable Energy, Vehicle Technologies Office.

References

- [1] Q.Y. Wang, G.F. Li, B. Zhao, M.Q. Shen, R.X. Zhou, *Appl. Catal. B: Environ.* 101 (2010) 150–159.
- [2] F. Gao, J.H. Kwak, J. Szanyi, C.H.F. Peden, *Top. Catal.* 56 (2013) 1441–1459.
- [3] L.Y. Yang, S.Y. Lin, X. Yang, W.M. Fang, R.X. Zhou, *J. Hazard. Mater.* 279 (2014) 226–235.
- [4] S.K. Matam, E.H. Otal, M.H. Aguirre, A. Winkler, A. Ulrich, D. Rentsch, A. Weidenkaff, D. Ferri, *Catal. Today* 184 (2012) 237–244.
- [5] F. Gao, Y.L. Wang, N.M. Washton, M. Kollar, J. Szanyi, C.H.F. Peden, *ACS Catal.* 5 (2015) 6780–6791.
- [6] K.A. Michalow-Mauke, Y. Lu, K. Kowalski, T. Graule, M. Nachtegaal, O. Krocher, D. Ferri, *ACS Catal.* 5 (2015) 5657–5672.
- [7] Z.S. Zhang, B.B. Chen, X.K. Wang, L. Xu, C. Au, C. Shi, M. Crocker, *Appl. Catal. B: Environ.* 165 (2015) 232–244.
- [8] Y.X. Zhang, M. Meng, F.F. Dai, T. Ding, R. You, *J. Phys. Chem. C* 117 (2013) 23691–23700.
- [9] L. Olsson, E. Fridell, *J. Catal.* 210 (2002) 340–353.
- [10] S.S. Mulla, N. Chen, L. Cumaranatunge, G.E. Blau, D.Y. Zemlyanov, W.N. Delgass, W.S. Epling, F.H. Ribeiro, *J. Catal.* 241 (2006) 389–399.
- [11] S. Liu, M.T. Zhang, Y.Q. Huang, K.F. Zhao, Z.Y. Gao, M.J. Wu, Y.M. Dong, T. Wang, J.L. Shi, D.N. He, *RSC Adv.* 4 (2014) 29180–29186.
- [12] E. Park, M. Kim, H. Jung, S. Chin, J. Jurng, *ACS Catal.* 3 (2013) 1518–1525.
- [13] D.M. Meng, W.C. Zhan, Y. Guo, Y.L. Guo, L. Wang, G.Z. Lu, *ACS Catal.* 5 (2015) 5973–5983.
- [14] W.C. Wang, G. McCool, N. Kapur, G. Yuan, B. Shan, M. Nguyen, U.M. Graham, B.H. Davis, G. Jacobs, K. Cho, X.H. Hao, *Science* 337 (2012) 832–835.
- [15] Z. Shu, Y. Chen, W.M. Huang, X.Z. Cui, L.X. Zhang, H.R. Chen, G.B. Zhang, X.Q. Fan, Y.X. Wang, G.J. Tao, D.N. He, J.L. Shi, *Appl. Catal. B: Environ.* 140–141 (2013) 42–50.
- [16] Z. Shu, W.M. Huang, Z. Hua, L.X. Zhang, X.Z. Cui, Y. Chen, H.R. Chen, C.Y. Wei, Y.X. Wang, X.Q. Fan, H.L. Yao, D.N. He, J.L. Shi, *J. Mater. Chem. A* 1 (2013) 10218–10227.
- [17] Y.Y. Du, Z.L. Hua, W.M. Huang, M.Y. Wu, M. Wang, J. Wang, X.Z. Cui, L.X. Zhang, H.R. Chen, J.L. Shi, *Chem. Commun.* 51 (2015) 5887–5889.
- [18] W.M. Huang, J.L. Shi, *Appl. Catal. A: Gen.* 507 (2015) 65–74.
- [19] N. Takahashi, H. Shinjoh, T. Iijima, T. Suzuki, K. Yamazaki, K. Yokota, H. Suzuki, N. Miyoshi, S. Matsumoto, T. Tanizawa, T. Tanaka, S. Tateishi, K. Kasahara, *Catal. Today* 27 (1996) 63–69.
- [20] E. Fridell, M. Skoglundh, B. Westerberg, S. Johansson, G. Smedler, *J. Catal.* 183 (1999) 196–209.
- [21] A. Yamamoto, Y. Mizuno, K. Teramura, S. Hosokawa, T. Tanaka, *ACS Catal.* 5 (2015) 2939–2943.
- [22] B. Grzybowska, J. Słoczyński, R. Grabowski, K. Wcislo, A. Kozłowska, J. Stoch, J. Zieliński, *J. Catal.* 178 (1998) 687–700.
- [23] J. Sainio, M. Eriksson, J. Lahtinen, *Surf. Sci.* 532–535 (2003) 396–401.
- [24] G.P. Halada, C.R. Clayton, *J. Electrochem. Soc.* 138 (1991) 2921–2927.
- [25] D.L. Hoanga, A. Dittmar, J. Radnik, K.W. Brzezinka, K. Witke, *Appl. Catal. A: Gen.* 239 (2003) 95–110.
- [26] A. Trunschke, D.L. Hoang, J. Radnik, H. Lieske, *J. Catal.* 191 (2000) 456–466.
- [27] N. Russo, D. Fino, G. Saracco, V. Specchia, *J. Catal.* 229 (2005) 459–469.
- [28] C. Boucetta, M. Kacimi, A. Ensuque, J.Y. Piquemal, F.B. Verduraz, M. Ziyad, *Appl. Catal. A: Gen.* 356 (2009) 201–210.
- [29] L.C. Wang, Q. Liu, M. Chen, Y.M. Liu, Y. Gao, H.Y. He, K.N. Fan, *J. Phys. Chem. C* 111 (2007) 16549–16557.
- [30] Z.H. Chen, Q. Yang, H. Li, X.H. Li, L.F. Wang, S.C. Tsang, *J. Catal.* 276 (2010) 56–65.
- [31] L. Ovari, S.K. Calderon, Y. Lykhach, J. Libuda, A. Erdohelyi, C. Papp, J. Kiss, H.P. Steinruck, *J. Catal.* 307 (2013) 132–139.
- [32] J. Faye, A. Baylet, M. Trentesaux, S. Royer, F. Dumeignil, D. Duprez, S. Valange, J.M. Tatibouet, *Appl. Catal. B: Environ.* 126 (2012) 134–143.
- [33] R.P. Vasquez, *J. Electron Spectrosc. Relat. Phenom.* 56 (1991) 217–240.
- [34] E. Ozensoy, C.H.F. Peden, J. Szanyi, *J. Phys. Chem. B* 109 (2005) 15977–15984.
- [35] Z.X. Liu, K. Xie, Y.Q. Li, Q.X. Bao, *J. Catal.* 119 (1989) 249–251.
- [36] B. Penkala, D. Aubert, H. Kaper, C. Tardivat, K. Conder, W. Paulus, *Catal. Sci. Technol.* 5 (2015) 4839–4848.
- [37] M. Schraml-Marth, A. Wokaun, A. Baiker, *J. Catal.* 138 (1992) 306–321.
- [38] K.I. Hadjivanov, D.G. Klissurski, V. Ph Bushev, *J. Chem. Soc. Faraday Trans.* 91 (1995) 149–153.
- [39] L.Y. Wu, S.R. Tong, M.F. Ge, *J. Phys. Chem. A* 117 (2013) 4937–4942.
- [40] Y. Peng, C.X. Liu, X.Y. Zhang, J.H. Li, *Appl. Catal. B: Environ.* 140–141 (2013) 276–282.
- [41] F. Cao, J. Xiang, S. Su, P.Y. Wang, L.S. Sun, S. Hu, S.Y. Lei, *Chem. Eng. J.* 243 (2014) 347–354.
- [42] E.L. Kugler, A.B. Kadet, J.W. Gryder, *J. Catal.* 41 (1976) 72–81.